AIAA JOURNAL
Vol. 49, No. 7, July 2011

Computational Study of Microflaps with Application to Vibration Reduction in Helicopter Rotors

Li Liu,* Ashwani K. Padthe,† and Peretz P. Friedmann‡
University of Michigan, Ann Arbor, Michigan 48109

DOI: 10.2514/1.J050829

A comprehensive study on unsteady effects of oscillating Gurney flaps, or microflaps, has been conducted. Two-dimensional unsteady airloads for lift, moment, and drag due to an oscillating microflap were computed using a compressible Reynolds-averaged Navier–Stokes flow solver. The computational fluid dynamics results were generated with an overset-mesh approach that captures oscillatory microflap motion. Three microflap configurations were examined to determine the type most suitable in terms of actuation efficiency and practical implementation. Furthermore, a reduced-order model for the unsteady microflaps was developed based on computational fluid dynamics simulations, using the rational function approximation approach. The resulting rational function approximation model is a state-space time-domain aerodynamic model that accounts for unsteadiness, compressibility, and time-varying freestream effect. The agreement between the reduced-order model and direct computational fluid dynamics calculations was found to be excellent for a wide range of flow conditions examined. The approximate model is suitable for incorporation in a comprehensive code, from which the potential of microflaps for active control of vibrations in rotors can be determined. Open-loop control studies indicated that the microflap produces substantial vibration reduction (80% reduction in vertical shear), whereas closed-loop control using combined harmonic inputs consisting of a sum of four harmonics (2–5/rev) reduced the vibration objective by 92%, on a hingeless rotor configuration resembling the Messerschmitt-Bölkow-Blohm BO-105. These results confirmed the control authority and effectiveness of the microflap for vibration reduction in rotorcraft.

Nomenclature

A	=	unsteady amplitude
b	=	airfoil semichord $=c/2$
C_d	=	total drag coefficient
C_{hm}	=	hinge moment coefficient
$\mathbf{C}_i$	=	rational function coefficient matrices $(\mathbf{C}_0, \mathbf{C}_1, \ldots, \mathbf{C}_{n+1})$
C_l	=	lift coefficient
C_m	=	moment coefficient
C_T	=	rotor thrust coefficient
c	=	airfoil chord
c_f	=	microflap chord
$\mathbf{D}$, $\mathbf{E}$, $\mathbf{R}$	=	matrices defined in the rational function approximation model
D_0, D_1	=	generalized flap motions
F_{HX4}, F_{HY4}, F_{HZ4}	=	nondimensional 4/rev hub shears
$\mathbf{f}$	=	generalized load vector
$\mathbf{G}$	=	Laplace transform of $\mathbf{f}(\bar{t})U(\bar{t})$
$\mathbf{H}$	=	Laplace transform of $\mathbf{h}(\bar{t})$
h	=	airfoil plunge coordinate
$\mathbf{h}$	=	generalized motion vector
K	=	kernel function in Possio's integral
k	=	reduced frequency $\omega b/U$
L/D	=	lift-to-drag ratio
L_b	=	blade length
L_c	=	spanwise dimension of blade segment with microflap
M	=	Mach number
M_{HX4}, M_{HY4}, M_{HZ4}	=	nondimensional 4/rev hub moments
N_b	=	number of rotor blades
n_L	=	number of lag terms
$\bar{p}$	=	nondimensional surface pressure distribution
$\mathbf{Q}$	=	aerodynamic transfer function matrix
$\tilde{\mathbf{Q}}$	=	approximation of $\mathbf{Q}$
s	=	Laplace variable
$\bar{s}$	=	nondimensional Laplace variable sb/U
t	=	time
$\bar{t}$	=	reduced time $\frac{1}{b}\int_0^t U(\tau)\,\mathrm{d}\tau$
$U(t)$	=	freestream velocity, time-dependent
W_0, W_1	=	generalized airfoil motions
$\mathbf{x}(t)$	=	aerodynamic state vector
x_c	=	spanwise location of center of microflap segment
α	=	airfoil angle of attack
β_p	=	blade precone angle
δ_f	=	microflap deployment amplitude
γ	=	Lock number
γ_n	=	rational approximant poles
θ_{tw}	=	built-in blade pretwist angle
μ	=	helicopter advance ratio
σ	=	rotor solidity
ϕ_c	=	phase angle
Ω	=	rotor angular speed
ω	=	oscillation frequency
$\bar{\omega}$	=	nondimensional normal velocity distribution
ω_F, ω_L, ω_T	=	blade flap, lag, and torsional natural frequencies

This paper received the ASME/Boeing Best Paper Award in April 2010, for the best paper presented at the 50th AIAA/ASME/ASCE/AHS/ASC Structures, Structural Dynamics, and Materials Conference; presented as Paper 2009-2604 at the 50th AIAA/ASME/ASCE/AHS/ASC Structures, Structural Dynamics, and Materials Conference, Palm Springs, CA, 4–7 May 2009; received 4 August 2010; revision received 21 December 2010; accepted for publication 15 February 2011.

*Research Fellow, Department of Aerospace Engineering. Senior Member AIAA.

†Ph.D. Candidate, Department of Aerospace Engineering. Student Member AIAA.

‡François-Xavier Bagnoud Professor, Department of Aerospace Engineering. Fellow AIAA.

I. Introduction

HIGH-LIFT devices are widely used to improve the performance of modern aircraft. The Gurney flap, originally conceived by Dan Gurney to increase the downward force generated by the spoiler on his race car, has emerged as a useful high-lift device in aeronautics. Unlike other high-lift devices, which often consist of a combination of several elements linked together, the Gurney flap is a small flap (typically 1–5%c in chord) and is attached normal to the airfoil pressure surface at the trailing edge, as shown in Fig. 1. Depending on its size and location, the Gurney flap is capable of increasing the maximum lift coefficient of an airfoil by up to 30%, based on experiments conducted at Reynolds numbers over 1×10^6 [1–3]. One of the earliest experimental studies on aerodynamics of a Gurney flap was conducted by Liebeck [4], who hypothesized that the Gurney flap caused the flow to turn around the trailing edge, resulting in the formation of two counter-rotating vortices behind the flap, shown in Fig. 1. The turning of the flow shifts the trailing-edge stagnation point to the bottom edge of the microflap, thus changing the Kutta condition and increasing the effective camber of the airfoil. Subsequently, the effectiveness of the Gurney flap has also been confirmed using computational fluid dynamics (CFD) simulations [2,5–7]. These studies have shown that despite their small size, Gurney flaps can increase the maximum lift, as well as the lift produced at any given angle of attack.

Active Gurney flaps that are deployable as opposed to being permanently fixed are referred to as microflaps in this study. This device has the potential for high bandwidth control with low-actuation power requirements, minimal loss in structural stiffness of the wing, and lower-wing warping when compared with the conventional control surfaces. Microflaps have been studied for various applications such as flutter suppression of high-aspect-ratio flexible wings, aeroelastic control of a blended-wing–body configuration, wing trailing-edge vortex alleviation, aerodynamic load control for wind turbine blades, and rotorcraft performance enhancement [7–17]. It was found in [8] that the deployable microflaps can increase flutter speed of a highly flexible wing by up to 22%. Another study [9] has proposed the use of microflap for control of aeroelastic response at the wing tip of a flexible blended-wing–body configuration. Recent studies for fixed-wing applications [10–12] suggest that microflaps can also be used for wake manipulation by inducing time-varying perturbations that excite vortex instability in the wake. The potential of microflaps with application to active load control in wind turbine blades was explored computationally and experimentally on representative turbine airfoil sections [7,13]. Substantial reduction in turbine blade root bending moment (reduction of peak bending moment ranging from 30–50%) was observed in [14] using microflaps. In [14] the microflap effect was simulated based on static Gurney flap measurements. Preliminary studies on rotorcraft performance enhancement using permanently attached Gurney flaps (size of less than 2%c) have been conducted in [15]. The effect of Gurney flaps on the airfoil lift and drag was modeled as a curve fit of experimental results obtained for flap having various sizes in terms of airfoil chord. Wind-tunnel tests conducted on a model helicopter confirmed that Gurney flaps may have beneficial effects on rotorcraft performance. More recently, deployable microflaps have been studied with active control strategies to enhance rotorcraft performance [16,17]. A relatively simple deployment schedule where the microflaps are deployed primarily on retreating side of the disk was used, and the maximum thrust of the rotor was enhanced by 6%.

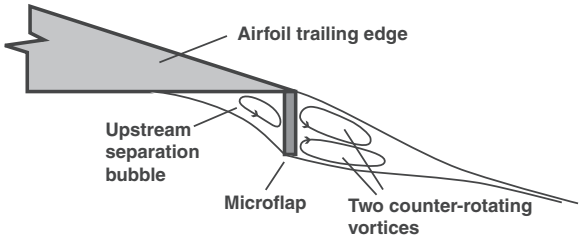

Fig. 1 Illustration of the Gurney flap.

During the last 15 years, various active control approaches, including conventional plain trailing-edge flaps, have been found to be effective for vibration reduction in rotorcraft [18–23]. The size advantage of the microflap when compared with the plain flaps will allow high bandwidth actuation with small actuation power, and thus it is a potentially attractive candidate for active control of helicopter vibration. However, a comprehensive and systematic assessment of the potential of microflaps for vibration reduction has not been conducted. As mentioned earlier, CFD tools can be used to determine unsteady aerodynamic characteristics of the microflap with reasonable accuracy. However, the computational costs are prohibitive when conducting parametric trend studies involving active control. Therefore, a reduced-order aerodynamic model is essential for the conduct of studies aimed at determining the vibration-reduction characteristics of microflaps for rotary-wing applications. Furthermore, such a reduced-order aerodynamic model has to be expressed in the time domain and has a mathematical form represented by ordinary differential equations that are suitable for coupling with equations of motion used for modeling the structural dynamics of the helicopter rotor in a comprehensive rotorcraft simulation code. The so-called comprehensive rotorcraft code refers to a general-purpose rotorcraft analysis system that contains a broad range of modeling capabilities and can be used to analyze blade airloads, aeroelastic responses/stability, rotor trim, vibratory loads and/or noise, performance, etc. Examples of comprehensive codes are RCAS [24], CAMRAD II [25], and UMARC [26].

The rational function approximation (RFA) approach has been used in the past to generate a Laplace transform or state variable representation of the unsteady aerodynamic loading on a wing section for fixed-wing applications [27–30] and rotary-wing applications [31]. Myrtle and Friedmann [31] have adapted and extended this approach to rotary-wing applications. They have employed a two-dimensional doublet-lattice (DL) method to obtain the 2-D unsteady aerodynamic loading on a cross section consisting of a blade/oscillating-flap combination. Subsequently, the RFA approach was used to convert the loads from the frequency domain to the time domain. The resulting aerodynamic model, denoted here as the RFA model, is an unsteady compressible state-space aerodynamic model, which has several important features:

1) It allows a convenient combination of the aerodynamics with the structural dynamic model.

2) It is suitable for the solution of the combined system, which is governed by equations with periodic coefficients, since it facilitates the use of direct numerical integration.

3) It provides a degree of computational efficiency required by the implementation of active control techniques such as trailing-edge flaps.

This RFA model has been implemented in a comprehensive rotorcraft simulation code [32] used in several computational studies involving the effect of active flaps on helicopter vibration and noise reduction, as well as performance enhancement [19,22,33]. The DL method is based on linear potential flow theory and thus cannot predict the drag coefficient or account for the airfoil-thickness effects. Furthermore, the flow characteristics behind a deployed microflap, which are dominated by viscous effects, cannot be determined by the DL method. These limitations are overcome in the present study by using a compressible unsteady Reynolds-averaged Navier–Stokes CFD solver to generate the frequency-domain unsteady aerodynamic loads. These CFD-based loads replace the DL based frequency-domain unsteady loads used in earlier studies of actively controlled flaps.

The overall objectives of this study are to enhance our fundamental understanding of the aerodynamic effects introduced by microflaps under both steady and dynamic conditions and develop a CFD-based nonlinear reduced-order aerodynamic model for microflaps that is suitable for incorporation into a comprehensive rotorcraft simulation. The specific objectives are as follows:

1) Conduct a numerical study of the microflap under steady and dynamic conditions using CFD, and determine the effects of the microflap on lift, moment, and drag coefficients of a 2-D airfoil.

2) Study and compare the aerodynamic properties of various oscillating microflap configurations using time-accurate Navier–Stokes simulations and identify the configuration most suitable for implementation in rotorcraft applications.

3) Develop a CFD-based nonlinear reduced-order aerodynamic model for the microflap configuration that is suitable for incorporation into a comprehensive rotorcraft simulation code.

4) Combine the reduced-order microflap aerodynamic model with comprehensive rotorcraft simulation code, and examine the potential of the microflap for helicopter vibration reduction, in both open- and closed-loop modes.

Clearly, achieving these goals will substantially advance the fundamental understanding of the physics of microflaps and allow one to assess the potential of the microflap as a viable device for active control of vibrations in rotorcraft.

II. CFD Solver and Grid Geometries

The CFD results generated in this study are obtained using CFD++ [34,35] developed by Metacomp Technologies. The CFD++ code is capable of solving the compressible unsteady Reynolds-averaged Navier–Stokes equations. It uses a unified-grid methodology that can handle a variety of structured, unstructured, and multiblock meshes and cell types, including patched and overset-grid features. Spatial discretization of the Navier–Stokes equations is based on a second-order multidimensional total-variation-diminishing scheme [36]. For the temporal scheme, a first-order implicit algorithm with dual time-stepping is employed to perform time-dependent flow simulations, with multigrid convergence acceleration. Several turbulence models are available in CFD++, ranging from one-equation to three-equation transport models. The k-ω shear-stress transport model [37] is used in the present study for turbulence modeling, due to its favorable performance in separated flow. All the computations are carried out assuming fully turbulent flow.

Both steady and time-accurate flow simulations are performed to examine the aerodynamic characteristics of the microflap combined with a NACA0012 airfoil, with the principal emphasis on unsteady effects of the oscillating microflap. Three candidate configurations are examined and compared in order to identify a microflap configuration suitable for practical implementation. Furthermore, the effectiveness of the microflap configurations for generating unsteady airloads is assessed. The grids employed for studying the different microflap configurations are shown in Figs. 2a–2c. Grids for the various microflap configurations are generated using the overset approach, which is particularly convenient for modeling complex geometries and moving components with large relative motions. The first configuration consists of a microflap that slides in and out from a cavity located at a given distance upstream from the sharp trailing edge of the airfoil, as shown in Fig. 2a. This configuration is similar to that employed in [7,38]. The grid for this configuration is obtained by successive combination of several overset refinement grids for the microflap and the cavity, as shown in the figure. The second configuration consists of a microflap that moves up and down behind the blunt trailing edge of the airfoil, shown in Fig. 2b. The blunt trailing edge is created by removing the aft portion of the airfoil such that there is enough space for accommodating the microflap when in the fully retracted position. The third microflap configuration has a rotational hinge at the trailing edge and thus resembles a miniature plain flap, as shown in Fig. 2c.

The airfoil grids for the microflap configurations are based on a grid refinement study conducted in [39] for unsteady trailing-edge flap simulations. The total number of grid points for the three microflap configurations depicted in Figs. 2a–2c, is 120,000, 138,000, and 124,000, respectively. The computational domain is a C-grid with far field boundary extending to 50 chord lengths in all directions. The grids are clustered at the airfoil wall boundaries such that the dimensionless distance y^+ of the first grid point off the wall is less than 1 and the equations are solved directly to the walls.

A direct validation of time-accurate CFD simulations for oscillating microflaps cannot be conducted, due to the lack of unsteady microflap experiments. Therefore, the CFD predictions for a 1.5%c Gurney flap under steady conditions are compared with experimental data obtained in [40]. The airfoil is NACA0012 and the 1.5%c Gurney flap is located 6%c upstream of the airfoil trailing edge, on the pressure side of the airfoil. This configuration is similar to the sharp-trailing-edge configuration depicted in Fig. 2a. The experiments were conducted at a freestream Mach number of approximately 0.1 and the Reynolds number is 2.1×10^6.

The aerodynamic effects of the Gurney flap are shown in Fig. 3, comparing the sectional lift, moment, and drag for the airfoil equipped with the 1.5%c Gurney flap against those for a clean airfoil. It is evident from Figs. 3a and 3b that the lift and moment predictions of the Gurney flap are in reasonable agreement with the experiments in the angle of attack range below stall. In particular, the differences in the lift and moment due to the Gurney flap when compared with the clean airfoil are well captured by CFD. Note that the stall onset angles predicted by CFD significantly exceed those obtained in the experiments for both the clean airfoil and the airfoil with the Gurney flap. The disagreement in the stall onset predictions with experiments may be attributed to the limitations of the turbulence model, as well as the fact that boundary-layer transition is not considered in the CFD

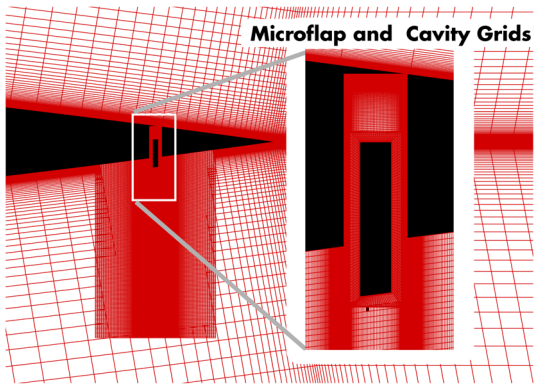

a) Sliding microflap in a cavity

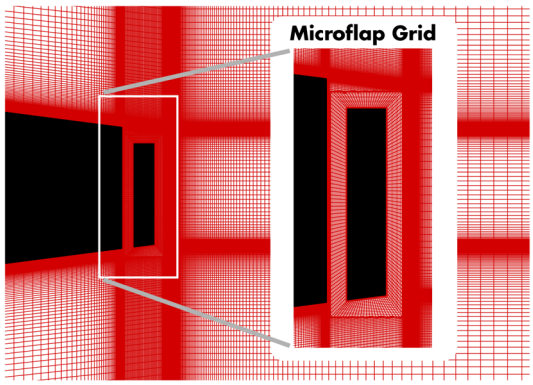

b) Sliding microflap at blunt trailing edge

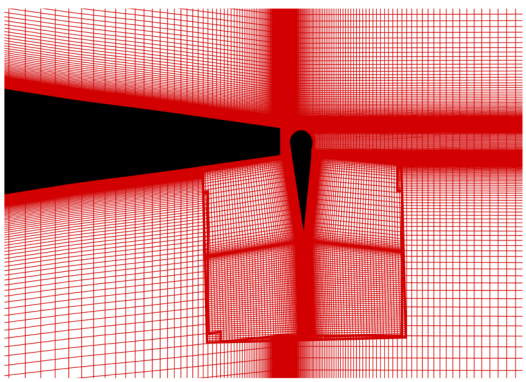

c) Rotating microflap resembling a plain flap

Fig. 2 Three candidate microflap configurations.

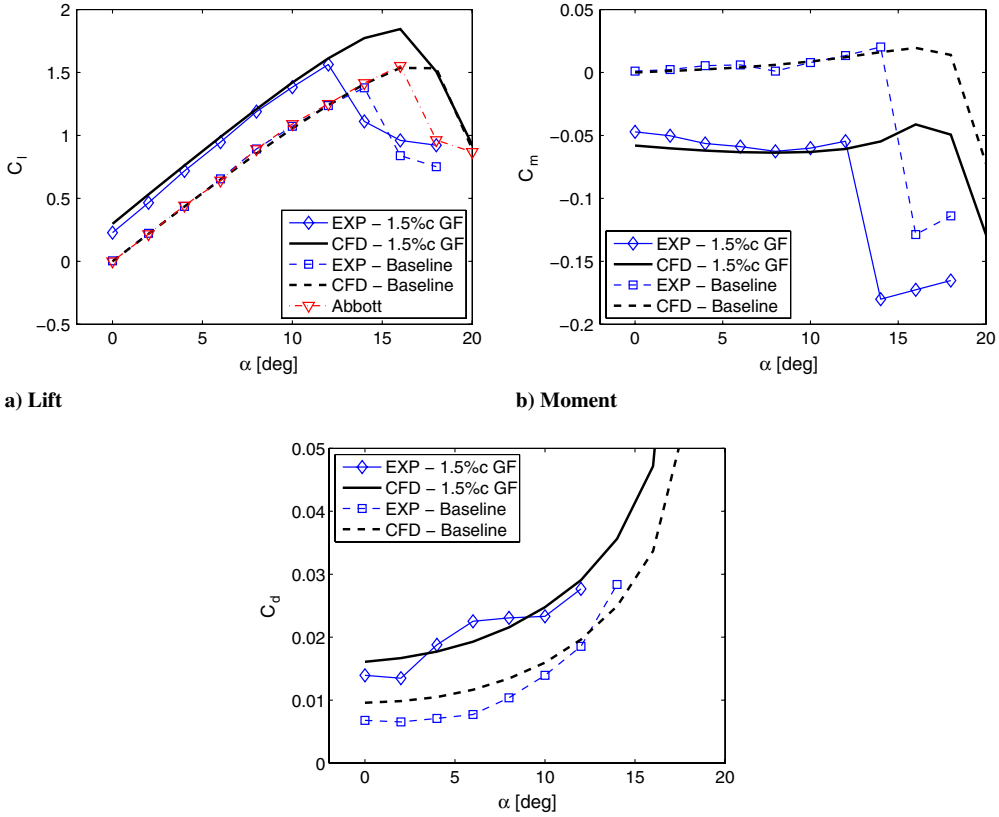

Fig. 3 Comparisons of static forces and moments due to Gurney flap to experiments for a 1.5%c Gurney flap located 6%c upstream of the TE; $M = 0.1$.

calculations, where the boundary layer is assumed to be fully turbulent. It is also important to note that the onset of stall is influenced by a number of factors such as freestream turbulence level, airfoil skin roughness, etc., as evidenced by the fact that there is a large variance in the stall angle among various experiments found in the literature. Figure 3a also depicts the lift curve for a clean NACA0012 airfoil under flow conditions similar to those obtained from another experiment [41] (triangles), which shows a stall onset angle closer to the CFD prediction.

The drag predictions are shown in Fig. 3c, where the drag for the baseline clean airfoil is overpredicted for angles below stall by the CFD, which is mainly due to the fact that boundary-layer transition is not considered in the CFD calculations and the boundary layer is assumed to be fully turbulent. The drag overprediction by CFD when compared with experimental data was also noted in [17]. The overall trend for the increased drag due to the 1.5%c Gurney flap when compared with the baseline airfoil is in reasonable agreement with the experiments.

III. Reduced-Order Model for Microflaps

The development of the RFA-based reduced-order model (ROM) for microflaps is presented in this section. It is a state-space time-domain model that accounts for flow unsteadiness and compressibility. In our earlier research, RFA-based aerodynamics were developed for modeling the aerodynamic response of a two-dimensional airfoil/trailing-edge flap combination. This unsteady aerodynamic model was implemented in a comprehensive rotorcraft simulation code AVINOR (Active Vibration and Noise Reduction), which has been carefully validated [22,32,42]. Recently, the accuracy of this model was also verified by comparing the RFA predictions with CFD-based results for the unsteady aerodynamic loads on two-dimensional airfoil/oscillating-flap combinations over a wide range of aerodynamic conditions representative of rotorcraft applications [39,43]. The RFA model was found to provide reasonable estimates of unsteady airloads for Mach numbers below $M = 0.70$. Clearly, the approximate RFA-based airloads require a very small amount of computer time when compared with CFD simulations.

A. Brief Description of the RFA Model

The RFA model developed in [31] is based on Rogers's approximation [27] for representing aerodynamic loads in the Laplace domain:

$$\mathbf{G}(\bar{s}) = \mathbf{Q}(\bar{s})\mathbf{H}(\bar{s}) \tag{1}$$

where $\mathbf{G}(\bar{s})$ and $\mathbf{H}(\bar{s})$ represent Laplace transforms of the generalized aerodynamic load and generalized motion vectors, respectively. The aerodynamic transfer matrix $\mathbf{Q}(\bar{s})$ is approximated using the least-squares approach with a rational expression of the form

$$\tilde{\mathbf{Q}}(\bar{s}) = \mathbf{C}_0 + \mathbf{C}_1\bar{s} + \sum_{n=1}^{n_L} \frac{\bar{s}}{\bar{s} + \gamma_n}\mathbf{C}_{n+1} \tag{2}$$

Equation (2) is usually denoted as the Rogers approximation. The poles $\gamma_1, \gamma_2, \ldots, \gamma_{n_L}$ are assumed to be positive valued to produce

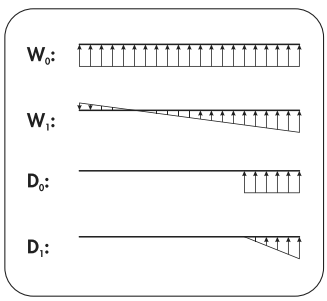

Fig. 4 Normal velocity distribution corresponding to generalized airfoil and flap motions.

stable open-loop roots, but are noncritical for the approximation. The arbitrary motions of the airfoil and the flap are represented by four generalized motions shown in Fig. 4. The normal velocity distributions shown in Fig. 4 correspond to two generalized airfoil motions (denoted by W_0 and W_1) and two generalized flap motions (denoted by D_0 and D_1). To find the least-squares approximants for the aerodynamic response, tabulated oscillatory airloads (i.e., sectional lift, moment, and hinge moment) have to be obtained, corresponding to each of the four generalized motions. In the original RFA implementation [31], the oscillatory airloads in the frequency domain were obtained from a two-dimensional DL solution [44] of Possio's integral equation [45], which relates pressure $\bar{p}$ to surface normal velocity $\bar{w}$, as indicated in Eq. (3):

$$\bar{w}(x) = \frac{1}{8\pi}\int_{-1}^{1} \bar{p}(\zeta)K(M, x-\zeta)\,\mathrm{d}\zeta \tag{3}$$

where K is the kernel function. This approach was found to be very efficient for generating a set of aerodynamic response data for the generalized motions of airfoil/flap combination. The frequency-domain information is generated for an appropriate set of reduced frequencies and Mach numbers, encompassing the entire range of unsteady flow conditions encountered in practical applications. The state-space representation of the RFA aerodynamic model requires a generalized motion vector $\mathbf{h}$ and produces a generalized load vector $\mathbf{f}$, defined as

$$\mathbf{h} = \begin{Bmatrix} W_0 \\ W_1 \\ D_0 \\ D_1 \end{Bmatrix}, \qquad \mathbf{f} = \begin{Bmatrix} \mathrm{C}_l \\ \mathrm{C}_m \\ \mathrm{C}_{\mathrm{hm}} \end{Bmatrix} \tag{4}$$

The Laplace transform representation in Eq. (1) relates the generalized motion to the generalized forces through the following expressions:

$$\mathbf{G}(\bar{s}) = \mathcal{L}[\mathbf{f}(\bar{t})U(\bar{t})], \qquad \mathbf{H}(\bar{s}) = \mathcal{L}[\mathbf{h}(\bar{t})] \tag{5}$$

The reduced time $\bar{t}$ is defined such that unsteady freestream effects can be properly accounted for [31] and may be interpreted as the distance traveled by the airfoil measured in semichords. The rational approximant $\tilde{\mathbf{Q}}$ in Eq. (2) can be transformed to the time domain using the inverse Laplace transform, which yields the final form of the state-space model, given in Eqs. (6) and (7):

$$\dot{\mathbf{x}}(t) = \frac{U(t)}{b}\mathbf{R}\mathbf{x}(t) + \mathbf{E}\dot{\mathbf{h}}(t) \tag{6}$$

$$\mathbf{f}(t) = \frac{1}{U(t)}\left(\mathbf{C}_0\mathbf{h}(t) + \mathbf{C}_1\frac{b}{U(t)}\dot{\mathbf{h}}(t) + \mathbf{D}\mathbf{x}(t)\right) \tag{7}$$

where the matrices $\mathbf{D}$, $\mathbf{R}$, and $\mathbf{E}$ are given by

$$\mathbf{D} = [\,\mathbf{I} \quad \mathbf{I} \quad \cdots \quad \mathbf{I}\,], \qquad \mathbf{R} = -\begin{bmatrix} \gamma_1\mathbf{I} & & & \\ & \gamma_2\mathbf{I} & & \\ & & \ddots & \\ & & & \gamma_{n_L}\mathbf{I} \end{bmatrix}$$

$$\mathbf{E} = \begin{bmatrix} \mathbf{C}_2 \\ \mathbf{C}_3 \\ \vdots \\ \mathbf{C}_{n_L+1} \end{bmatrix}$$

B. Modified RFA Model for the Microflap Configuration

The DL method is based on linear potential flow theory; as a result, the RFA model constructed based on oscillatory responses generated using the DL method is no longer valid when significant flow nonlinearities associated with viscous effects or shock wave formation are present. As mentioned earlier, flow characteristics of a fully deployed microflap are governed by viscous effects and therefore cannot be predicted from the DL method. Furthermore, unsteady drag due to the microflap motion, which is important for estimating the performance penalty due to such devices, cannot be obtained from potential flow theory. Therefore, the frequency-domain solutions required for the construction of the RFA model are obtained from a compressible unsteady Reynolds-averaged Navier–Stokes (RANS) solver, CFD++. Thus, the viscous interactions governing the flow behind a microflap can be properly determined. Furthermore, in this approach the unsteady drag is also computed, in addition to the lift and moment. When using this approach, the generalized load vector $\mathbf{f}$ is written as

$$\mathbf{f} = \begin{Bmatrix} C_l \\ C_m \\ C_d \end{Bmatrix} \tag{8}$$

In the present study, the hinge moment of the microflap was not needed and therefore is not computed.

When constructing the RFA model for an airfoil with microflap, two generalized airfoil motions represented by W_0 and W_1, shown in Fig. 4, are used to describe arbitrary airfoil pitch and plunge motion. In terms of classical pitch and plunge coordinates α and h, these generalized motions are expressed as

$$W_0 = U\alpha + \dot{h} \tag{9}$$

$$W_1 = b\dot{\alpha} \tag{10}$$

Thus, the description of the airfoil motion is identical to that used in the original RFA model. For the microflap, the concept of normal velocity distributions is no longer meaningful; therefore, the microflap is simply characterized by one generalized motion, namely, the deflection δ_f, where the deflection represents the deployment amplitude or the angular deflection, depending on the microflap configuration. The generalized motion D_1, used in the original RFA model to describe the motion of conventional flaps, is no longer used. This is justified because the generalized motion D_1 primarily represents the apparent mass effect, which is found to be insignificant for the microflap in the CFD simulations. Therefore, the generalized motion vector $\mathbf{h}$ for the microflap is expressed as

$$\mathbf{h} = \begin{Bmatrix} W_0 \\ W_1 \\ D_0 \end{Bmatrix} \tag{11}$$

where

$$D_0 = \delta_f \tag{12}$$

To account for flow nonlinearities encountered at high Mach numbers, large angles of attack, and large amplitudes of microflap deployment or angular deflection (in the case of the configuration shown in Fig. 2c), the RFA model is modified by using a technique referred to as *model scheduling* [46]. In this approach the different sets of RFA coefficients are generated at appropriate combinations of the Mach number, angle of attack, and microflap deployment amplitude or angular deflection. This procedure resembles the gain scheduling approach commonly used in nonlinear control system design [46,47]. Specifically, the RFA model is modified by allowing the coefficient matrices, as represented by $\mathbf{R}, \mathbf{E}, \mathbf{C}_0, \mathbf{C}_1, \ldots$, to vary with M, α, and δ_f. The resulting state-space model in the time domain can now be written in the form given by Eq. (13):

$$\begin{aligned} \dot{\mathbf{x}}(t) &= \frac{U(t)}{b}\mathbf{R}(M,\alpha,\delta_f)\mathbf{x}(t) + \mathbf{E}(M,\alpha,\delta_f)\dot{\mathbf{h}}(t) \\ \mathbf{f}(t) &= \frac{1}{U(t)}\left(\mathbf{C}_0(M,\alpha,\delta_f)\mathbf{h}(t) + \mathbf{C}_1(M,\alpha,\delta_f)\frac{b}{U(t)}\dot{\mathbf{h}}(t)\right. \\ &\quad \left. + \mathbf{D}\mathbf{x}(t)\right) \end{aligned} \tag{13}$$

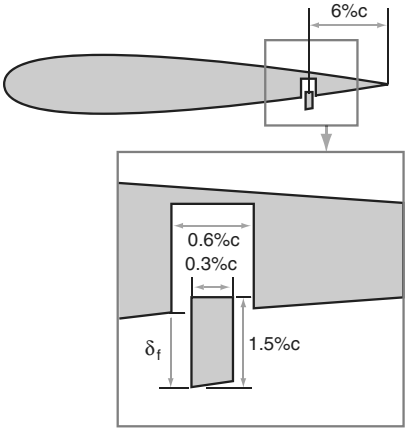

Fig. 5 Oscillating microflap in a cavity.

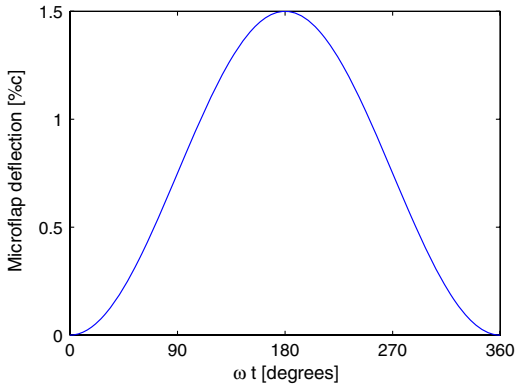

Fig. 6 Time history of unsteady microflap deflection.

In this new approach unsteady airloads in response to harmonic motions of W_0, W_1, and δ_f at selected values of reduced frequencies are generated using CFD. The use of the CFD code accounts for fully unsteady, combined airfoil and microflap motions.

IV. Results and Discussions

For all computations described in this section the Reynolds number is 3.36×10^6. In the computations, the flow is first allowed to reach steady state before conducting time-dependent simulations for various oscillating microflap configurations. The simulations are conducted using the overset-mesh approach based on the computational grids discussed earlier. The time steps used in the time-accurate simulations were selected to ensure that at least 250 points are present for each flap oscillation cycle, and at least four cycles are computed to ensure that periodicity has been achieved.

A. Steady and Oscillating Microflaps

The flow conditions and oscillating frequencies for the unsteady microflap simulations are selected to be representative of the aerodynamic environment encountered during the vibration control of a typical hingeless rotor, which resembles a hingeless rotor blade used on the Messerschmitt-Bölkow-Blohm (MBB) BO-105 helicopter. The freestream Mach number is 0.51. The unsteady microflap is examined at two values of reduced frequencies, namely, $k = 0.0688$ and 0.1376, based on airfoil chord. These oscillatory frequencies correspond to approximately 2/rev and 4/rev for the MBB BO-105 rotor, which has four blades, and for which such harmonics have been successfully used in active vibration control studies [18,19]. The airfoil is set to a 0° mean angle of attack. Results for various oscillating microflap configurations combined with a NACA0012 airfoil are presented next.

The first configuration consists of a microflap sliding in and out of a cavity, located at $6\%c$ upstream from the sharp trailing edge (TE) of the airfoil, as depicted in Fig. 5. The microflap is $1.5\%c$ in height, and the other relevant dimensions are also shown in the figure. Microflap deflection δ_f is defined as the distance from the end of the flap to the surface of the airfoil, as illustrated in Fig. 5. The microflap starts from a completely retracted position, i.e., $\delta_f = 0$, and slides out of the cavity to attain a maximum deflection of $\delta_f = 1.5\%c$. Simulations are conducted for the microflap undergoing sinusoidal oscillations, given by

$$\delta_f = A(1 - \cos \omega t) \tag{14}$$

where $A = 0.75\%c$ is the amplitude and ω is the frequency of oscillation. This deflection time history is shown in Fig. 6 for an oscillating frequency of $k = 0.0688$.

The unsteady lift as a function of nondimensional reduced time $\bar{t}$ is shown in Fig. 7a. The lift is also plotted as a function of the microflap deflection δ_f, shown in Fig. 7b. For comparison purposes, all the figures in this section showing unsteady aerodynamic coefficients also display the steady force coefficients for a fully deployed microflap, indicated in the figure by $\delta_f = 1.5\%c$. Similarly, steady values of lift when the microflap is fully retracted is identified as $\delta_f = 0\%c$. The maximum unsteady lift C_l at $k = 0.0688$ is significantly less than the steady lift, indicating lift deficiency due to unsteady effects. Oscillatory amplitude of the unsteady lift is further reduced when k is increased from 0.0688 to 0.1376. Variations of the unsteady moment coefficients with reduced time and microflap deflection are shown in Figs. 8a and 8b, respectively. From these figures, it can be seen that the effect of flow unsteadiness on the magnitude of the moment is fairly small. The drag coefficients as functions of reduced time and the microflap deflection are shown in Figs. 9a and 9b, respectively. Comparison of the unsteady effect on

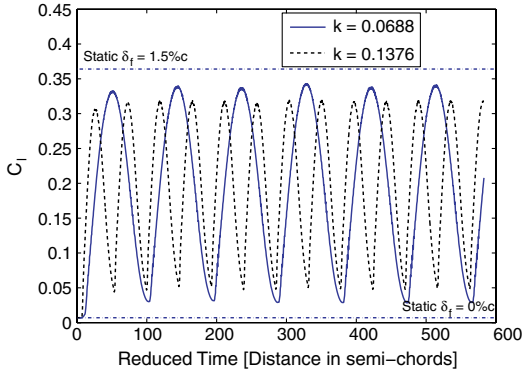

a) C_l vs. $\bar{t}$

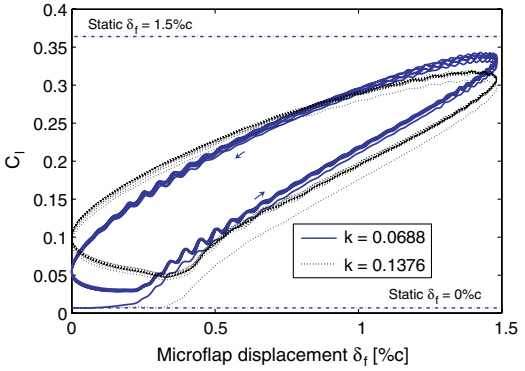

b) C_l vs. δ_f

Fig. 7 Unsteady lift for a $1.5\%c$ microflap at two reduced frequencies for the sharp-TE configuration; $M = 0.51$.

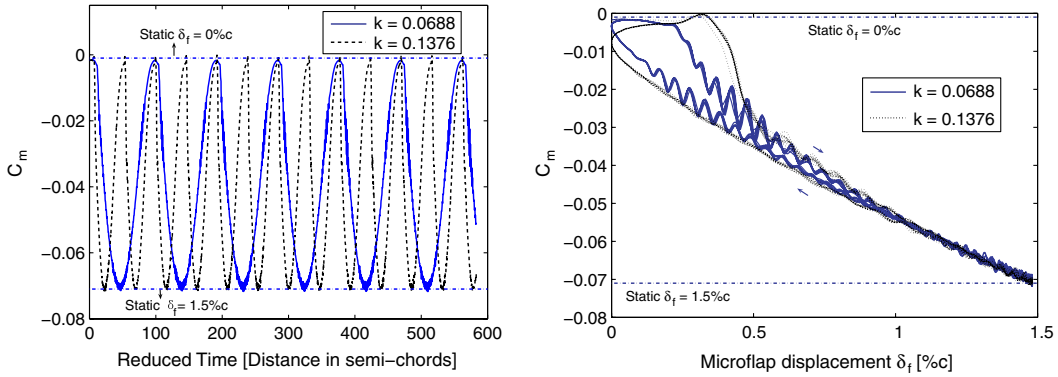

a) C_m vs. $\bar{t}$ **b) C_m vs. δ_f**

Fig. 8 Unsteady moment for a 1.5%c microflap at two reduced frequencies for the sharp-TE configuration; $M = 0.51$.

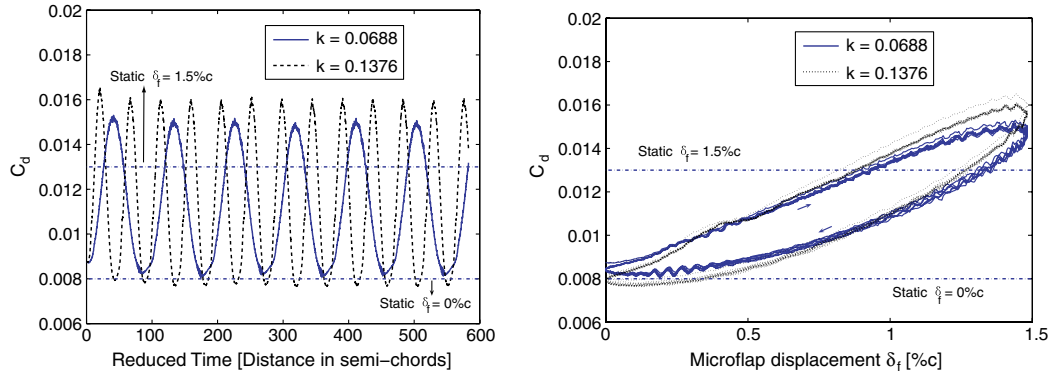

a) C_d vs. $\bar{t}$ **b) C_d vs. δ_f**

Fig. 9 Unsteady drag for a 1.5%c microflap at two reduced frequencies for the sharp-TE configuration; $M = 0.51$.

the oscillating amplitude at two frequencies shown in Fig. 9a indicates that microflaps oscillating at higher reduced frequencies produce a larger unsteady drag amplitude, which is a behavior that is contrary to the case shown earlier for unsteady lift.

A time lag in lift coefficient can be observed while the microflap is sliding out of the cavity, as the flow takes time to develop and form a vortical structure behind the microflap. This nonlinear behavior is evident in the time-history plots of the aerodynamic coefficients, which appear to have nonharmonic components, despite the fact that the microflap motion is purely harmonic, as given by Eq. (14).

The results for the second configuration consisting of an oscillating microflap located at the blunt trailing edge of the airfoil, shown in Fig. 10, are presented next. The blunt trailing edge is created by removing the aft 6% of the airfoil. This configuration has a potential advantage over the previous configuration because for this case the microflap can be deflected both up and down from its neutral position. Furthermore, this configuration may be easier to implement from a practical point of view, when the placement of the actuation mechanism is considered. For comparison purposes, the simulations were performed only with downward motion of the microflap, with similar flap deflection schedule to that given in Eq. (14). The flow parameters were also identical to those used for the previous configuration.

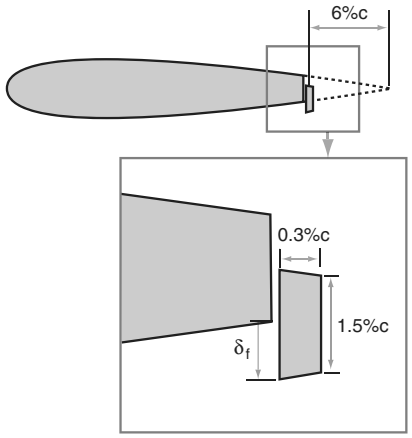

Fig. 10 Oscillating microflap at the blunt trailing edge.

Unsteady lift, moment, and drag due to the microflap motion are presented in a similar manner to those given earlier for the sharp-TE configuration. First, the lift coefficient is plotted against the reduced time and δ_f in Figs. 11a and 11b, respectively. The unsteady moments time histories are shown in Figs. 12a and 12b. Similar plots for the drag coefficient are also given in Figs. 13a and 13b. Again, the effect of flow unsteadiness associated with the two reduced frequencies used in the computations displays characteristics similar to those noted earlier for the first configuration. When comparing the drag associated with these two configurations, as shown in Figs. 9b and 13b, two observations can be made. The static drag for the sharp-edge configuration when the microflap is fully deployed is $C_d \cong 0.013$, whereas the static drag for the blunt-edge configuration is higher $C_d \cong 0.014$. When comparing the unsteady drag behaviors for the two configurations they appear to be quite similar and the difference between the two unsteady drag curves is smaller than the difference noted for the static drag. Another interesting difference between these two configurations is evident when one examines the unsteady lift shown in Figs. 7a, 7b, 11a, and 11b. Both the static and oscillatory lift produced by the sharp-edge configuration are significantly higher than those produced by the blunt-edge configuration.

The third flap configuration selected was a microflap that resembles a plain flap rotating at the TE, as illustrated in Fig. 14. This

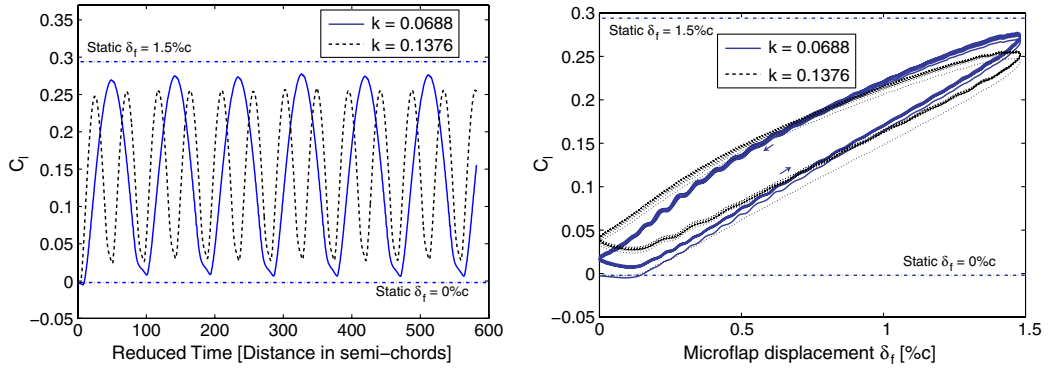

a) C_l vs. $\bar{t}$ b) C_l vs. δ_f

Fig. 11 Unsteady lift for a 1.5%c microflap oscillating at two reduced frequencies for the blunt-TE configuration; $M = 0.51$.

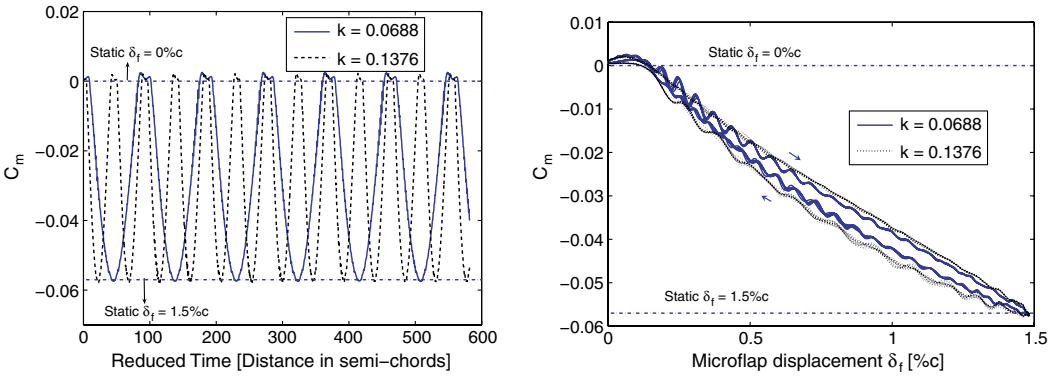

a) C_m vs. $\bar{t}$ b) C_m vs. δ_f

Fig. 12 Unsteady moment for a 1.5%c microflap oscillating at two reduced frequencies for the blunt-TE configuration; $M = 0.51$.

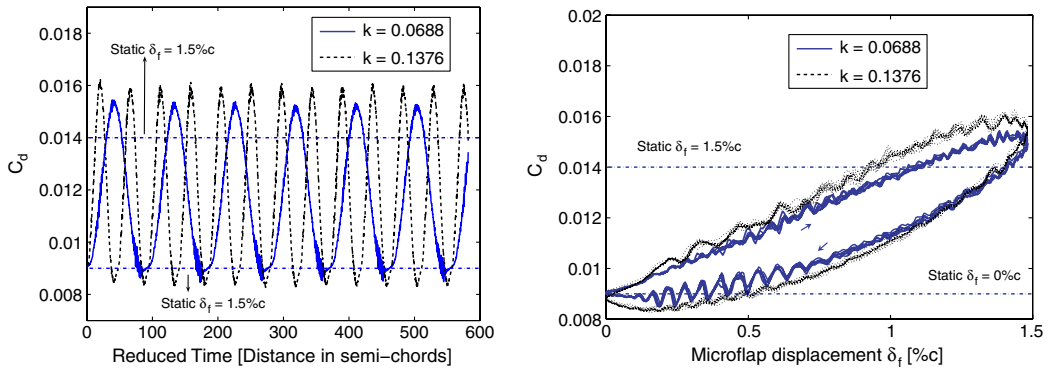

a) C_d vs. $\bar{t}$ b) C_d vs. δ_f

Fig. 13 Unsteady drag for a 1.5%c microflap oscillating at two reduced frequencies for the blunt-TE configuration; $M = 0.51$.

configuration may be difficult to implement in practice, due to space limitations for accommodating the actuators and hinges. To have a meaningful comparison with earlier results, the microflap is only rotated downward between $\delta_f = 0$ and 90°. Again, the simulated flow conditions are identical to those used for the previous two configurations.

For this configuration, the pressure contour plot near the trailing edge of the airfoil is shown in Fig. 15, along with the evolution of streamlines during one cycle of microflap oscillation. Figure 15 clearly illustrates the development of the vortical structure behind the microflap, which consists of two counter-rotating vortices when the microflap is fully deployed, and the pattern displayed in Fig. 15b is similar to that found on static Gurney flaps [6,48].

Comparisons of the unsteady lift, moment, and drag for all three oscillating microflap configurations are shown in Fig. 16 for

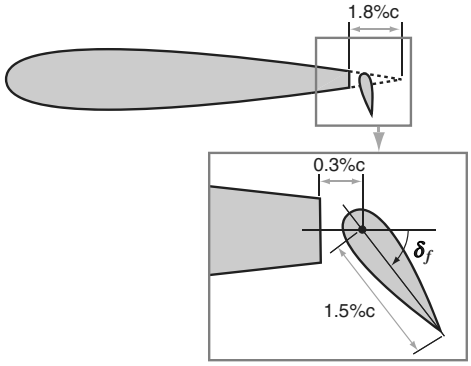

Fig. 14 Illustration of a rotating microflap resembling a plain flap.

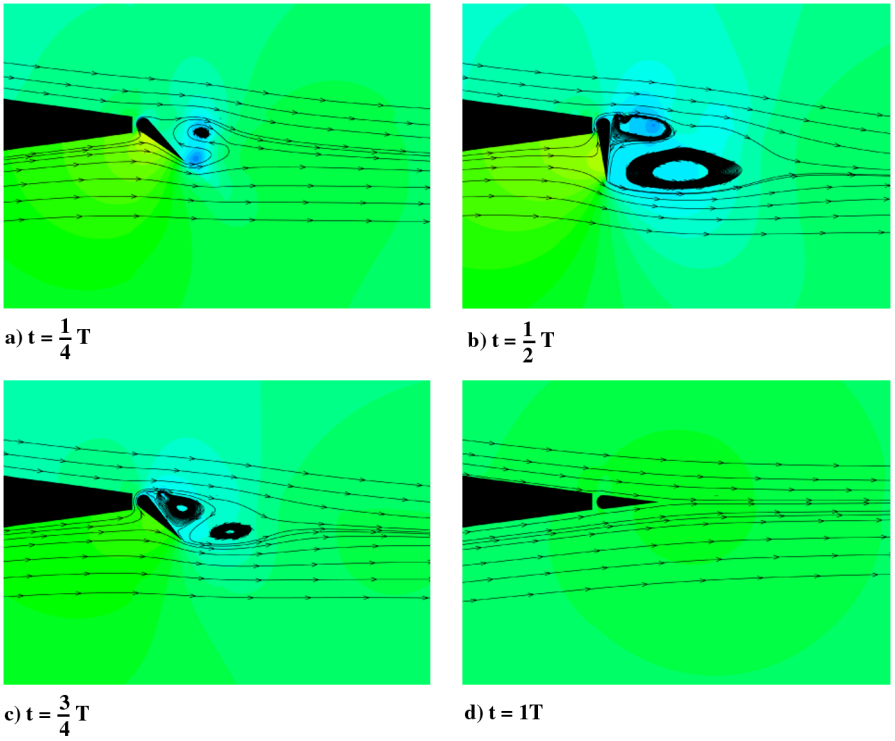

Fig. 15 Pressure contours and streamlines showing evolution of vortical structure during one cycle of oscillation behind the plain microflap at $M = 0.51$ and $\alpha = 0°$.

$k = 0.0688$ at the freestream Mach number of $M = 0.51$. The comparison in Fig. 16 indicates that the maximum lift when using the blunt-TE configuration is approximately 20% lower than that obtained with the sharp-TE configuration. The overall unsteady lift coefficient for the plain microflap configuration is similar to that for the blunt-TE configuration, except that at the maximum deflected position the plain microflap generates 17% less lift than that obtained with the blunt-TE configuration. The reason for the decrease in the maximum lift for the plain microflap can be attributed to the fact that the plain microflap in the 90° deflected position does not have the effective length of 1.5%c microflap, because the finite thickness of the airfoil trailing edge (see Fig. 14) reduces its effective length.

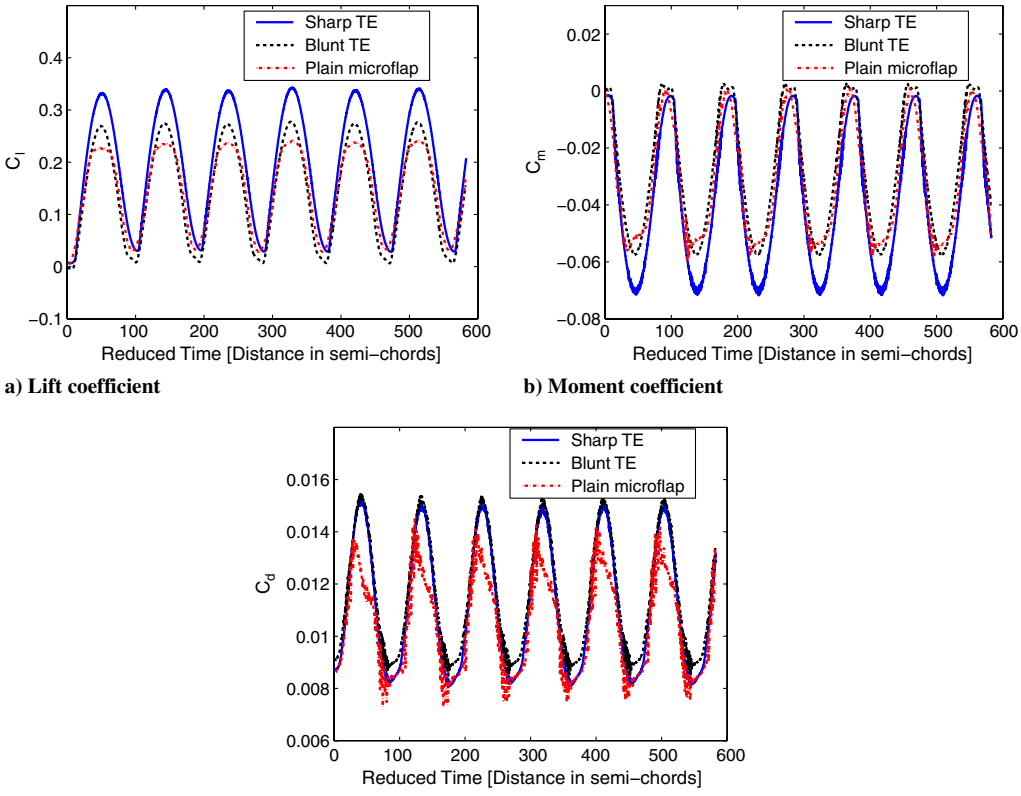

a) Lift coefficient

b) Moment coefficient

c) Drag coefficient

Fig. 16 Comparison of unsteady lift, moment, and drag for three different microflap configurations.

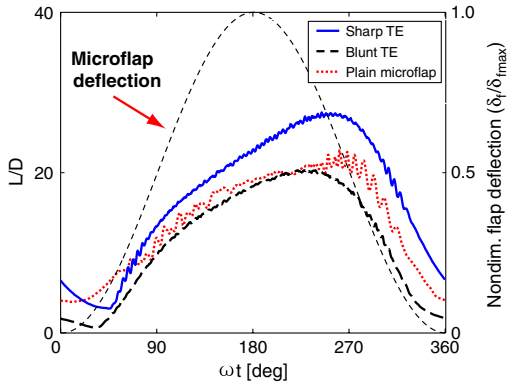

Fig. 17 Comparison of lift-to-drag ratio obtained for all three microflap configurations; $M = 0.6$ and $k = 0.0688$.

Comparison of moment coefficients reveals similar trends, which are again due to reduction in the effective length.

Figure 16c indicates that both sliding microflap configurations generate similar amounts of drag. By comparison, the plain microflap configuration produces the smallest amount of drag with a 7% decrease in the peak value when compared with the other two configurations. This reduction in drag is also due to the lower effective length of the plain microflap.

Variations of the lift-to-drag ratio during one deployment cycle associated with the three configurations are shown in Fig. 17, together with the normalized flap deflection time history. The configuration with the best L/D ratio is most desirable from a purely aerodynamic point of view. The results shown in Fig. 17, indicate that the sharp-TE configuration yields the best L/D ratio over the majority of the microflap deployment cycle, and the blunt-TE configuration is the worst. Overall, the sharp-TE configuration may be the best compromise between the aerodynamic benefits and the ease of implementation, provided that the structural strength of the blade is not adversely affected by the mechanical features of the microflap installation.

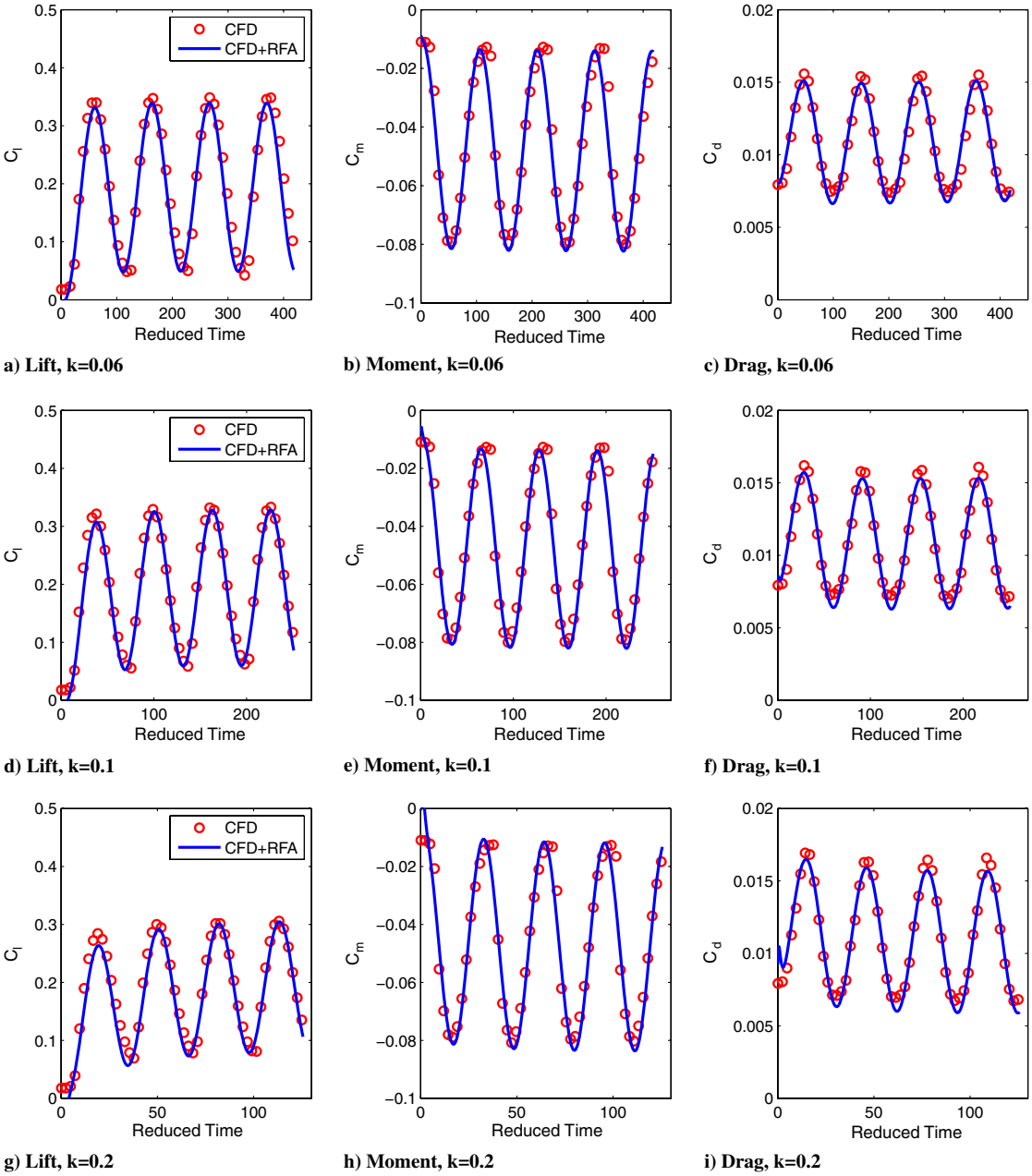

a) Lift, k=0.06 **b) Moment, k=0.06** **c) Drag, k=0.06**

d) Lift, k=0.1 **e) Moment, k=0.1** **f) Drag, k=0.1**

g) Lift, k=0.2 **h) Moment, k=0.2** **i) Drag, k=0.2**

Fig. 18 Unsteady force coefficients for an oscillating 1.5%c sharp-TE microflap with varying frequencies; $\alpha = 0°$ and $M = 0.6$.

B. Reduced-Order Model for Microflaps

Reduced-order models for sectional aerodynamic responses of microflaps are presented in this section. The ROMs are constructed using Eq. (13) except that in the present study the RFA coefficients generated for the ROMs are independent of the microflap deployment δ_f. To generate a ROM that can represent the entire range of flow conditions encountered by the blades at various advance ratios, CFD simulations are conducted for Mach numbers ranging from 0.05 to 0.9 and angles of attack ranging from 0° to 15°. At each flow condition defined by the freestream Mach number and the airfoil mean angle of attack, simulations are performed to generate frequency-domain data corresponding to the generalized motions at reduced frequency values ranging from 0.02 to 0.2 with an increment of 0.02. Note that the 5/rev frequency, which is the highest actuation frequency used for vibration reduction on a four-bladed rotor, corresponds to a reduced frequency value of approximately 0.18 based on the average local freestream velocity for a blade/microflap section at $0.75R$ span location. The microflap ROM developed using frequency-response data generated with CFD is referred to as the CFD + RFA model. The microflap configuration considered here is the sharp-trailing-edge type with a $1.5\%c$ microflap, as shown in Fig. 5.

To validate the ROMs, predictions from the CFD + RFA model are compared with direct CFD simulations for three reduced frequencies, at the Mach number of 0.6 and the airfoil angle of attack $\alpha = 0°$. Figures 18a, 18d, and 18g show the unsteady lift variation for the microflap oscillating motion given by Eq. (14) at three different reduced frequencies. The direct CFD results (circles) are compared with the ROM results (solid line). The agreement for all reduced frequencies shown here is excellent, and the ROM captures the unsteady lift deficiency effect when the reduced frequency is increased from 0.06 to 0.2. Similarly, the unsteady moment is also captured accurately by the ROM, as shown in Figs. 18b, 18e, and 18h. The unsteady drag predictions, shown in Figs. 18c, 18f, and 18i, are less accurate, since the ROM predictions exhibit some error in the mean values (less than 10%) when compared with the CFD calculations. This error in the mean value predictions may be reduced by using more CFD fitting points when generating the reduced-order

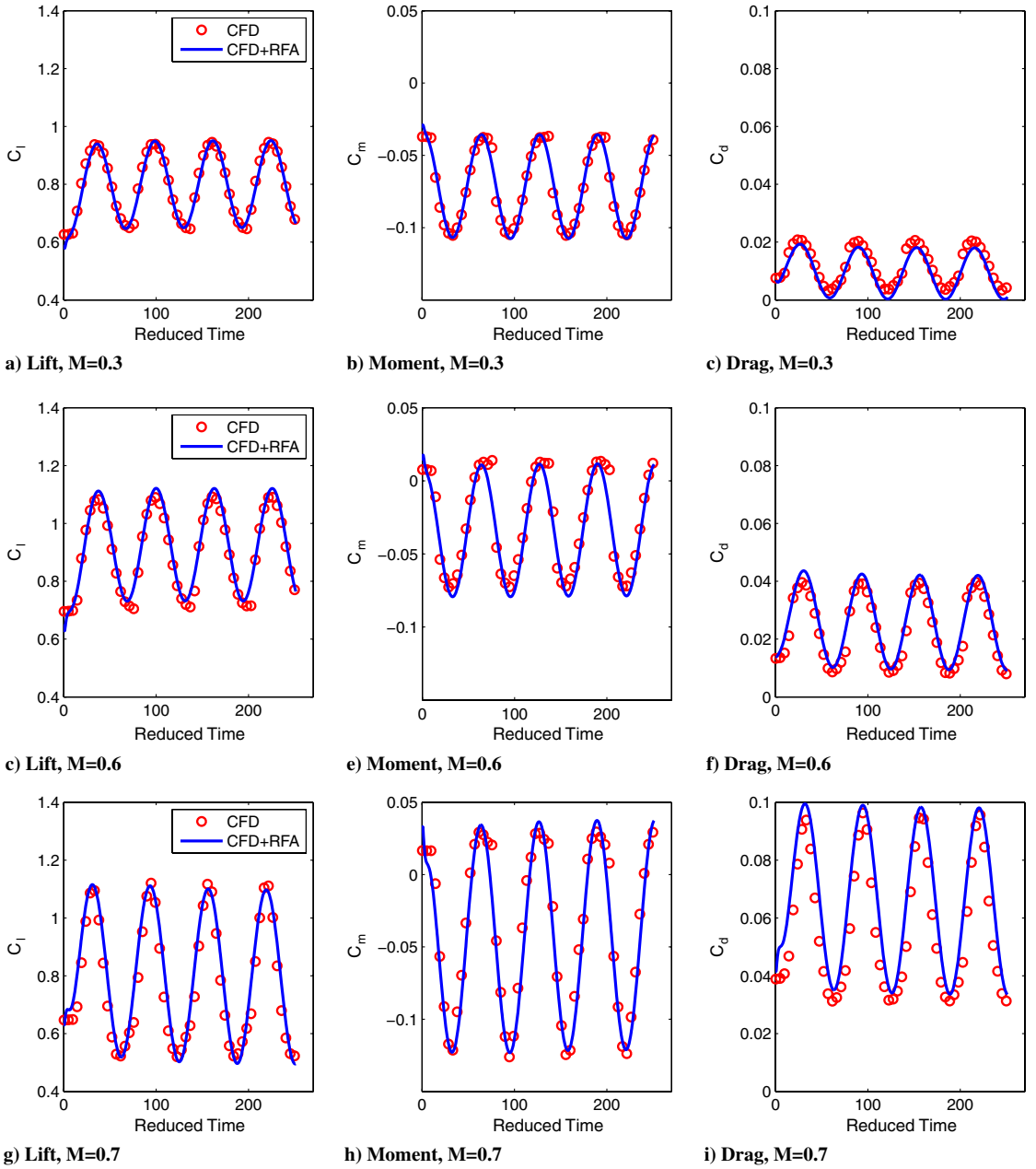

Fig. 19 Unsteady force coefficients for an oscillating $1.5\%c$ sharp-TE microflap with varying Mach numbers; $\alpha = 5°$ and $k = 0.1$.

model. Nevertheless, it is evident from Fig. 18 that the oscillating amplitudes of lift, moment, and drag coefficients due to the microflap motion are captured well.

Another set of results comparing the ROM predictions with direct CFD simulations at Mach numbers ranging from 0.3–0.7 is shown in Fig. 19. The airfoil angle of attack is $\alpha = 5°$ and the microflap oscillating frequency is $k = 0.1$. Although not shown, the comparisons for the other reduced frequency values of $k = 0.06$ and 0.2 at these Mach numbers and $\alpha = 5°$ exhibit a similar level of agreement between the ROM and the CFD results. These comparisons indicate that the ROM is accurate for the range of Mach numbers examined here.

The comparisons for the ROM and direct CFD simulations at airfoil angles of attack up to $\alpha = 10°$ are shown in Fig. 20 for $M = 0.6$ and $k = 0.1$. It is evident from Fig. 20 that the ROM fails to capture the strong nonlinear effects observed in the unsteady responses due to substantial flow separation, particularly at higher angles of attack ($\alpha = 8$ and 10°. Nevertheless, reasonable estimates in the mean values and oscillating magnitudes due to the microflap deflections are obtained.

Finally, comparisons of the ROM with direct CFD simulations conducted at an unsteady flow condition that is representative of rotorcraft aerodynamic environment are shown in Fig. 21. The combined motion of the airfoil and the microflap corresponds to a typical section on a rotor blade, with the airfoil rotating about the quarter-chord and the microflap deflecting simultaneously. The unsteady-motion time histories are plotted against the azimuth angle during one rotor revolution, shown in Figs. 21a–21c. The overall airfoil pitching motion includes the effect of geometric pitch setting (collective and blade pretwist), as well as 1/rev cyclic pitch angles for rotor control, shown in Fig. 21a. The microflap deflection consists of 2–5/rev harmonics (Fig. 21b), where each harmonic component is randomly phased with the same peak-to-peak amplitude of $0.4\%c$. Furthermore, the simultaneous airfoil/microflap motion is subject to freestream velocity variations, shown in Fig. 21c, representing the influence of helicopter forward speed. The lift, moment, and drag variations due to the combined motion are shown in Figs. 21d–21f. The baseline in Figs. 21d–21f denotes the case in which the airfoil has a pitching motion given by Fig. 21a and is subject to the freestream variation shown in Fig. 21c, but without the microflap

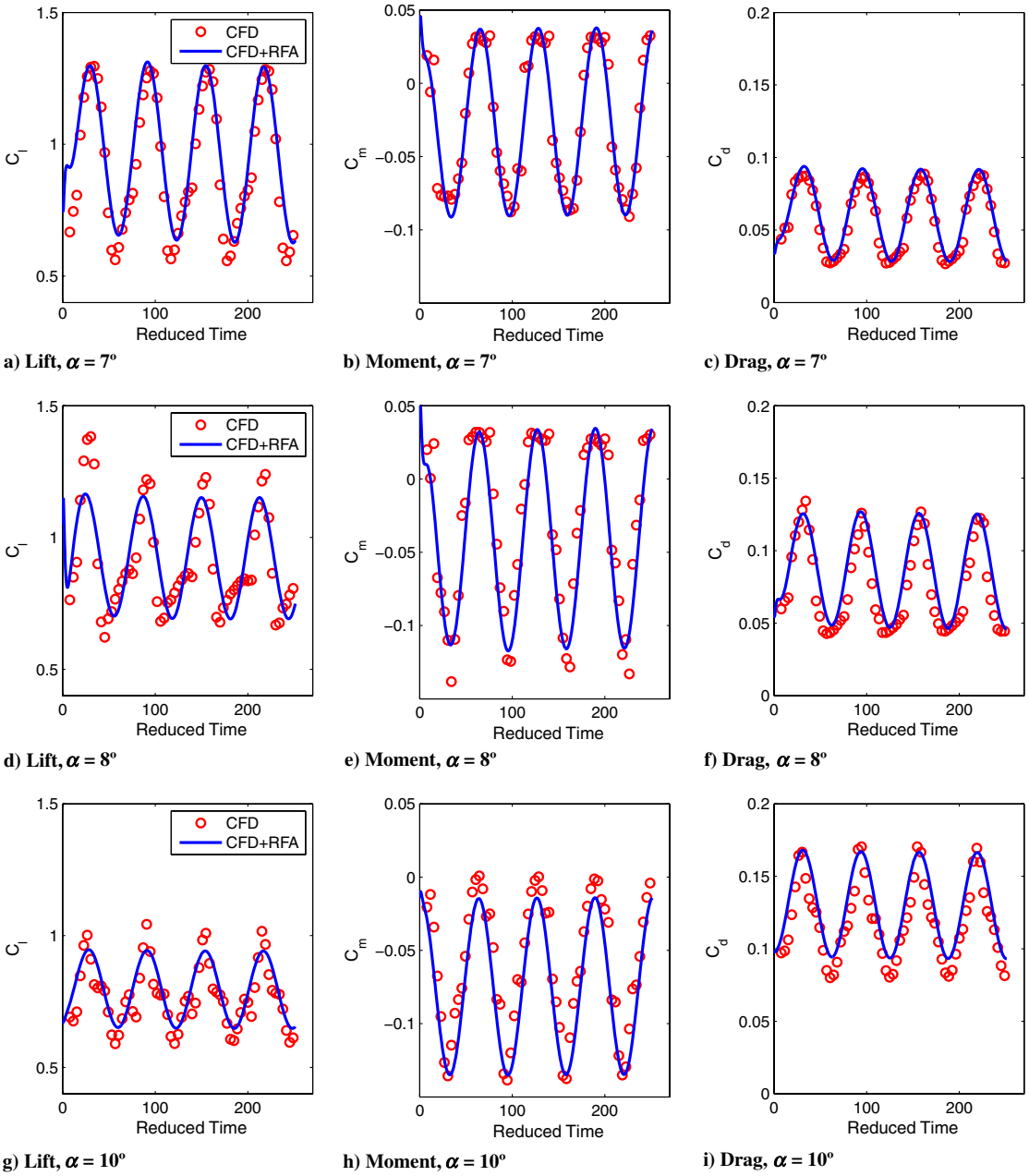

a) Lift, $\alpha = 7°$ b) Moment, $\alpha = 7°$ c) Drag, $\alpha = 7°$

d) Lift, $\alpha = 8°$ e) Moment, $\alpha = 8°$ f) Drag, $\alpha = 8°$

g) Lift, $\alpha = 10°$ h) Moment, $\alpha = 10°$ i) Drag, $\alpha = 10°$

Fig. 20 Unsteady force coefficients for an oscillating $1.5\%c$ sharp-TE microflap with varying airfoil angles of attack; $M = 0.6$ and $k = 0.1$.

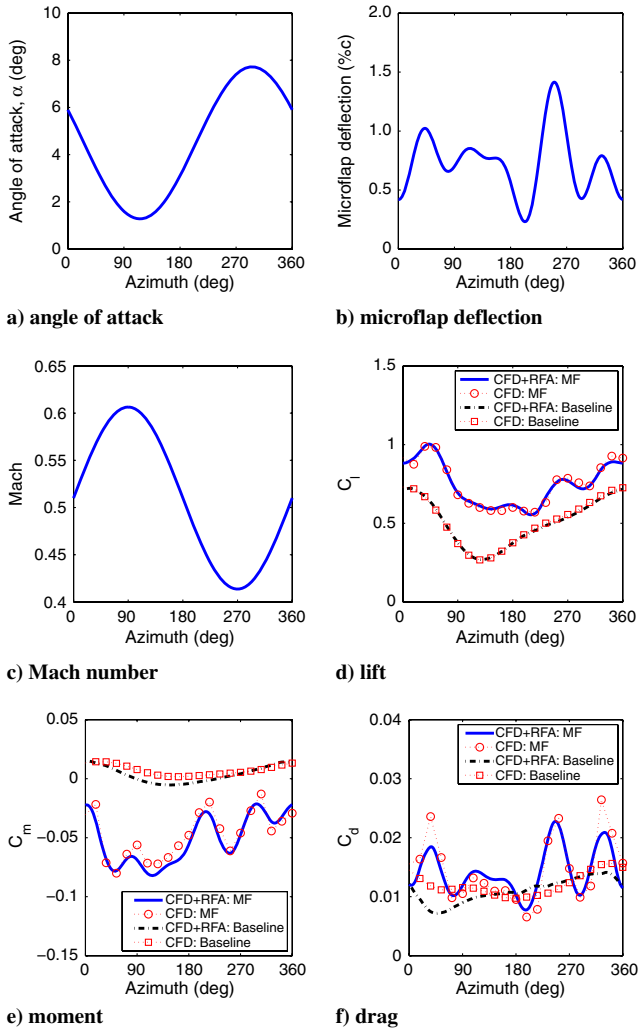

Fig. 21 Comparison of ROM predictions to direct CFD results for a 1.5%c sharp-TE microflap deflecting with randomly generated multiharmonic motion, at varying angles of attack subject to freestream velocity variations.

deflection, which is intended to be used to identify the effects of the microflap deflection. As can be seen from Fig. 21d, the unsteady lift predictions from the ROM, with or without microflap deflection, are in excellent agreement with the direct CFD calculations. It is also evident from Fig. 21e that the moment predictions agree quite well with the direct CFD results. The agreement in unsteady drag predictions (Fig. 21f) is not as good compared with lift and moment; however, the effect of the microflap on unsteady drag is captured, when comparing the unsteady drag due to the microflap to the baselines.

Overall, for a wide range of flow conditions representative of the operating conditions encountered in rotorcraft applications, the ROMs for the microflap provide excellent accuracy when compared with direct CFD calculations. Furthermore, the ability of the ROM to account for unsteady drag is a large improvement when compared with the original RFA model.

Table 1 Properties of the blade and microflap configuration

Parameters	Values
Rotor data	
N_b	4
ω_F	1.12, 3.41, 7.62
ω_L	0.73, 4.46
ω_T	3.17
θ_{tw}	−8°
γ	5.5
β_p	2.5°
c	$0.05498L_b$
σ	0.07
Helicopter data	
C_T/σ	0.0714
L_b	4.91 m
μ	0.15
Ω	425 rpm
Microflap configuration	
c_f	1.5%c
x_c	$0.75L_b$
L_c	$0.12L_b$

C. Vibration Reduction with the Microflap

The potential of microflap for vibration reduction on a representative hingeless rotor is studied by incorporating the ROM, described in the previous section, in a comprehensive rotorcraft simulation code. The microflap configuration considered is the sharp-TE configuration. The ROMs for unsteady lift, moment, and drag due to the microflap have been incorporated into the AVINOR code [32] to examine effects of the microflap on rotor blade vibration. The results provide a preliminary indication of the vibration-reduction capabilities of the microflap.

The vibratory hub shears and moments are obtained from the integration of the distributed inertial and aerodynamic loads over the entire blade span in the rotating frame. Subsequently, the loads are transformed to the hub-fixed nonrotating system, and the contributions from the individual blades are combined. In this process, the blades are assumed to be identical. Cancellation of various terms occurs and the dominant components of the hub shears and moments have a frequency of N_b/rev, which is the blade passage frequency. A propulsive trim procedure [49] is used where six equilibrium equations (three forces and three moments) for the entire helicopter in a steady forward flight condition are enforced. Additional details of the coupled trim/aeroelastic response solution procedure can be found in [32].

The rotor configuration considered is a four-bladed hingeless rotor, resembling the MBB BO-105. The advance ratio used in the simulations is $\mu = 0.15$ for steady level flight, which corresponds to a flight condition where high vibration levels are encountered due to strong blade–vortex interaction (BVI). Previous studies have been conducted using conventional actively controlled trailing-edge flaps for vibration reduction [22,31,42,49]. Therefore, one can compare (in an approximate manner) the vibration-reduction potential of the conventional flap and microflap under similar flight conditions. In this study, a single microflap is considered that spans 12% of the blade radius, centered at 75%R radial location. The spanwise size and location of the microflap configuration employed in the simulations are chosen such that they are identical to the single trailing-edge active flap configurations considered in earlier studies [50]. The properties of the rotor and microflap configurations are summarized in Table 1.

1. *Open-Loop Phase Sweep*

First, results simulating vibration reduction with the microflap operating in the open-loop mode were generated. An open-loop phase sweep is conducted by varying the phase angle ϕ_c for four discrete oscillating frequencies corresponding to 2/rev–5/rev, where the microflap motion is defined by

$$\delta_f = A[1 - \cos(\omega t + \phi_c)] \tag{15}$$

where $A = 0.75\%c$ for the 1.5%c microflap. The effect of the open-loop sweep on the 4/rev vertical hub shear vibratory component is examined. The 4/rev vertical shear component is chosen due to its correlation with the vibration levels felt at the pilot seat. Figure 22 shows the effects of each microflap harmonic on the 4/rev vertical shear. The results shown indicate the microflap control inputs significantly affect the 4/rev vertical shear. This suggests that the microflap has sufficient control authority for vibration reduction. It

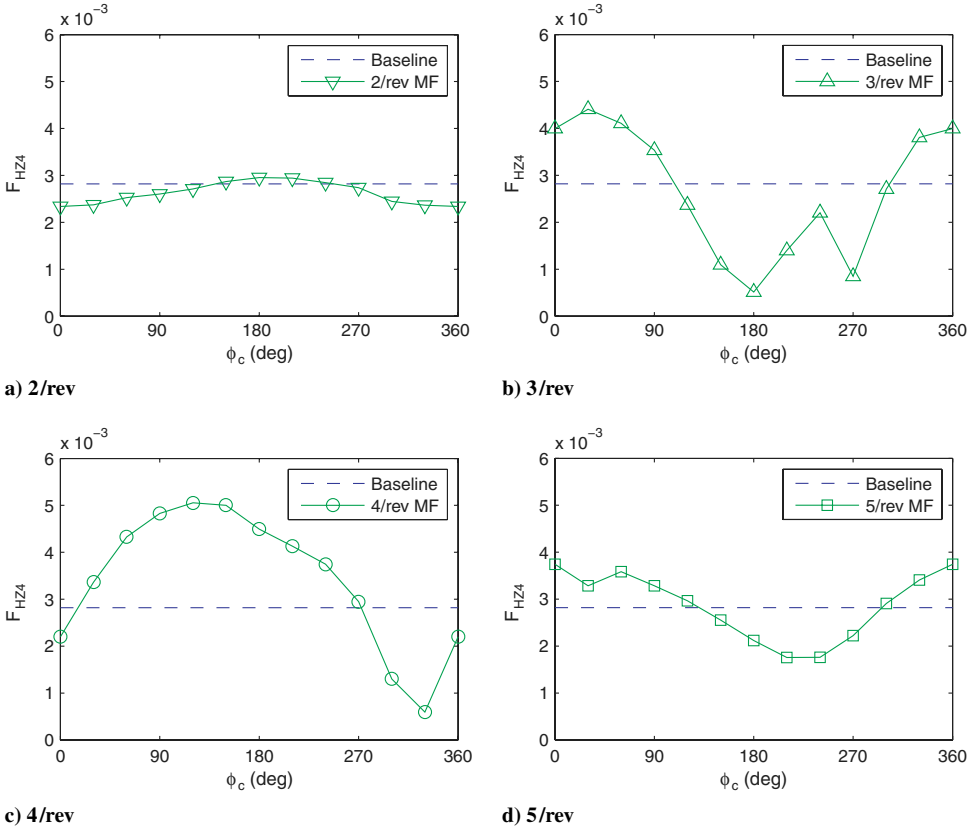

Fig. 22 Effect of phase sweep on 4/rev vertical hub shear F_{HZ4} with the microflap at $\mu = 0.15$.

was found that the 3/rev and 4/rev harmonics are most effective and capable of producing maximum vibration reduction of approximately 80%, at phase-angle settings of $\phi_c = 180$ and 330°, respectively. The 2/rev and 5/rev control inputs produce somewhat smaller vertical shear reduction levels, with maximum reductions of 17 and 38%, respectively. When compared with a conventional flap configuration with a servo flap having a chord of 25%c [50], which produced 90% maximum vibration reduction with 3/rev harmonics, the microflap generated a comparable amount of vibration reduction.

Vibratory hub loads for the 4/rev microflap harmonic input at phase angle $\phi_c = 330°$ are shown in Fig. 23, which corresponds to the maximum vertical shear reduction. Figure 23 shows all six components of the 4/rev hub loads, which consist of three hub shears and three hub moments. Although the vertical shear component F_{HZ4} is substantially reduced using this open-loop input, most other vibratory components are increased, which emphasizes the need for a combined vibration objective if simultaneous reduction of all vibratory components is desired.

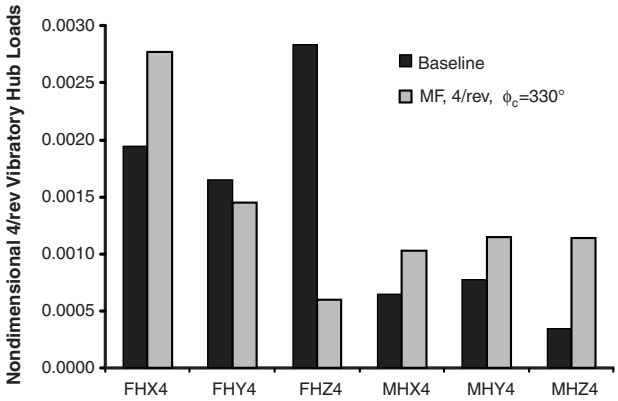

Fig. 23 Vibratory loads with the open-loop 4/rev microflap input at $\phi_c = 330°$.

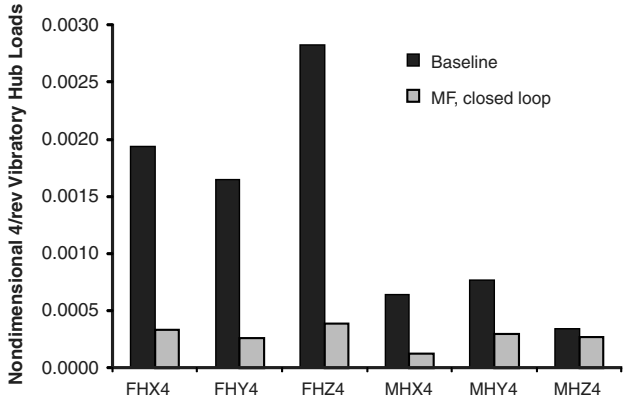

Fig. 24 The 4/rev vibratory hub shears and moments for the baseline and with microflap using closed-loop control at $\mu = 0.15$.

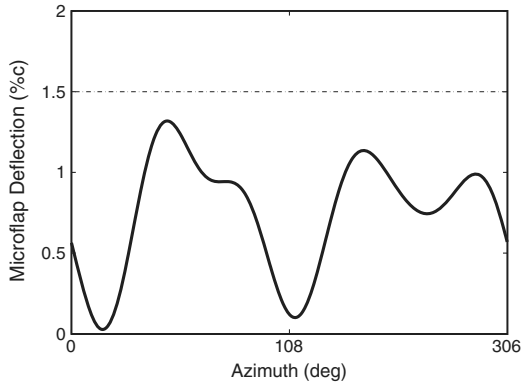

Fig. 25 Microflap deflection histories over one complete revolution during closed-loop control.

Table 2 Harmonic component breakdown of the optimal microflap deflection as determined by the closed-loop controller

Harmonic	Amplitude, %c	Phase, °
2/rev	0.37	344
3/rev	0.23	234
4/rev	0.23	282
5/rev	0.09	186

2. Closed-Loop Control

Vibration reduction using a feedback-controller-based on the higher harmonic control (HHC) algorithm [51] is conducted next using the microflap. The same microflap configuration, described earlier, is employed at the advance ratio of $\mu = 0.15$. The control input consists of a combination of the 2/rev, 3/rev, 4/rev, and 5/rev harmonic components of the microflap deflection. The control objective consists of a weighted sum of the squares of the 4/rev vibratory hub shears and moments, where the weightings for hub shears and moments are 1 and 10, respectively. The closed-loop HHC controller automatically selects the appropriate amplitude and phase angle for each frequency component (2–5/rev) of the microflap deflection through minimization of the objective function [51].

Vibratory hub loads corresponding to the baseline and controlled values are shown in Fig. 24. It is evident form the figure that the microflap produces a substantial amount of vibration reduction, clearly demonstrating the control authority of the microflap. The microflap reduced the combined vibration objective function by 92%, which is comparable with other active techniques such as the conventional trailing-edge flaps. The deflection history for the microflap over one complete revolution is shown in Fig. 25. Furthermore, the amplitudes and phase angles of the 2–5/rev harmonic components for the optimal microflap deflection are listed in Table 2. Note that the definitions of the amplitude and phase angle are identical to those defined in Eq. (15). It is evident that the phase angles for the 2–5/rev harmonics, determined by the closed-loop controller, are fairly close to the optimal phase angles found in the open-loop phase-sweep studies (see Fig. 22). Clearly, the closed-loop HHC controller is capable of finding an optimal control input that simultaneously reduces all six hub vibratory components.

V. Conclusions

The aerodynamic characteristics of three different microflap configurations were studied using the RANS flow solver, CFD++. The unsteady characteristics of the microflap were examined by considering several reduced frequencies representative of rotorcraft applications. Sectional aerodynamic responses for an oscillating microflap were obtained for three configurations: 1) a microflap sliding in and out of a cavity on an airfoil with sharp trailing edge, 2) a microflap sliding up and down at the blunt trailing edge of an airfoil, and 3) a microflap resembling a plain-flap configuration. The simulation results indicate that the configuration with sharp trailing edge yields the best L/D ratio and the blunt-TE configuration is the worst. However, the blunt-TE configuration may have an advantage when considerations associated with practical implementation are taken into account. Overall, the sharp-TE configuration may be the best compromise between the aerodynamic benefits and the ease of implementation.

A reduced-order aerodynamic model for the microflap was also developed, based on frequency-domain responses obtained from the CFD solver. The comparisons of the aerodynamic loads between the ROM and direct CFD calculations were excellent for unsteady compressible flow conditions that are characteristic of rotorcraft aerodynamic environment for most of the flow conditions explored in this study. In particular, good agreement has been obtained between the ROM and direct CFD predictions for a typical flow condition encountered by a blade section with simultaneous airfoil/microflap motion subject to freestream velocity variations. However, it is also noted that the ROM fails to capture strong nonlinear effects associated with airfoil stall. Nevertheless, the overall success of the CFD + RFA model in predicting efficiently and accurately the aerodynamic loading due to the microflaps indicates its suitability for incorporation into comprehensive rotorcraft simulation codes for investigation of the feasibility of microflaps for active control.

Active control studies aimed at determining the control authority of the microflaps for vibration reduction in rotorcraft were also conducted, by incorporating the ROMs developed in this study into a comprehensive rotorcraft simulation code. Open-loop phase-sweep studies confirmed that the microflap has sufficient control authority for vibration reduction, demonstrating more than 80% reduction in 4/rev vertical shear at a high-vibration BVI flight condition. Closed-loop control using input consisting of a combination of harmonics of 2–5/rev produced more than 90% reduction in the combined vibration objective function, further proving the effectiveness of the microflap for vibration reduction in rotorcraft.

Acknowledgments

This research was supported by the Vertical Lift Research Center of Excellence (VLRCOE) sponsored by the National Rotorcraft Technology Center (NRTC) and U.S. Army, with M. Rutkowski as grant monitor.

References

[1] Storms, B. L., and Jang, C. S., "Lift Enhancement of an Airfoil Using a Gurney Flap and Vortex Generators," *Journal of Aircraft*, Vol. 31, No. 3, May–June 1994, pp. 542–547. doi:10.2514/3.46528

[2] Baker, J. P., Standish, K. J., and van Dam, C. P., "Two-Dimensional Wind Tunnel and Computational Investigation of a Microtab Modified Airfoil," *Journal of Aircraft*, Vol. 44, No. 2, March–April 2007, pp. 563–572. doi:10.2514/1.24502

[3] Maughmer, M. D., and Bramesfeld, G., "Experimental Investigation of Gurney Flaps," *Journal of Aircraft*, Vol. 45, No. 6, Nov.–Dec. 2008, pp. 2062–2067. doi:10.2514/1.37050

[4] Liebeck, R. H., "Design of Subsonic Airfoils for High Lift," *Journal of Aircraft*, Vol. 15, No. 9, Sept. 1978, pp. 547–561. doi:10.2514/3.58406

[5] Giguere, P., Lemay, J., and Dumas, G., "Gurney Flap Effects and Scaling for Low-Speed Airfoils," *AIAA 13th Applied Aerodynamics Conference*, AIAA, Washington, D.C., 1995, pp. 966–976; also AIAA Paper 1995-1881, June 1995.

[6] Jang, C. S., Ross, J. C., and Cummings, R. M., "Numerical Investigation of an Airfoil with a Gurney Flap," *Aircraft Design*, Vol. 1, No. 2, June 1998, pp. 75–88. doi:10.1016/S1369-8869(98)00010-X

[7] Chow, R., and van Dam, C. P., "Unsteady Computational Investigations of Deploying Load Control Microtabs," *Journal of Aircraft*, Vol. 43, No. 5, Sept.–Oct. 2006, pp. 1458–1469. doi:10.2514/1.22562

[8] Lee, H.-T., Kroo, I. M., and Bieniawski, S., "Flutter Suppression for High Aspect Ratio Flexible Wings Using Microflaps," 43rd AIAA/ASME/ASCE/AHS/ACS Structures, Structural Dynamics and Materials Conf., Reno, NV, AIAA Paper 2002-1717, April 2002.

[9] Kroo, I. M., "Aerodynamic Concepts for Future Aircraft," 30th AIAA Fluid Dynamics Conf., Norfolk, VA, AIAA Paper 99-2003, June–July 1999.

[10] Matalanis, C. G., and Eaton, J. K., "Wake Vortex Alleviation Using Rapidly Actuated Segmented Gurney Flaps," *AIAA Journal*, Vol. 45, No. 8, Aug. 2007, pp. 1874–1884. doi:10.2514/1.28319

[11] Vey, S., Paschereit, O. C., Greenblatt, D., and Meyer, R., "Flap Vortex Management by Active Gurney Flaps," 46th AIAA Aerospace Sciences Meeting and Exhibit, Reno, NV, AIAA Paper 2008-286, Jan. 2008.

[12] Nikolic, V. R., "Two Aspects of the Use of Full- and Partial-Span Gurney Flaps," *Journal of Aircraft*, Vol. 44, No. 5, Sept.–Oct. 2007, pp. 1745–1748. doi:10.2514/1.29136

[13] Nakafuji, D. T. Y., van Dam, C. P., Smith, R. L., and Collins, S. D., "Active Load Control for Airfoils Using Microtabs," *Journal of Solar Energy Engineering*, Vol. 123, No. 4, Nov. 2001, pp. 282–289. doi:10.1115/1.1410110

[14] Wilson, D. G., Berg, D. E., Li, D. W., and Zayas, J. R., "Optimized Active Aerodynamic Blade Control for Load Alleviation on Large Wind Turbines," *AWEA Windpower 2008 Conference & Exhibition*, Houston, TX, June 2008.

[15] Kentfield, J. A. C., "The Potential of Gurney Flaps for Improving the Aerodynamic Performance of Helicopter Rotors," AIAA International Powered Lift Conf., AIAA Paper 1993-4883, Dec. 1993.

[16] Kinzel, M. P., Maughmer, M. D., and Lesieutre, G. L., "Miniature Trailing-Edge Effectors for Rotorcraft Performance Enhancement," *Journal of the American Helicopter Society*, Vol. 52, No. 2, April 2007, pp. 146–158. doi:10.4050/JAHS.52.146

[17] Kinzel, M. P., Maughmer, M. D., and Duque, E. P. N., "Numerical Investigation on the Aerodynamics of Oscillating Airfoils with Deployable Gurney Flaps," *AIAA Journal*, Vol. 48, No. 7, July 2010, pp. 1457–1469. doi:10.2514/1.J050070

[18] Friedmann, P. P., and Millott, T. A., "Vibration Reduction in Rotorcraft Using Active Control: A Comparison of Various Approaches," *Journal of Guidance, Control, and Dynamics*, Vol. 18, No. 4, July–Aug. 1995, pp. 664–673. doi:10.2514/3.21445

[19] Friedmann, P. P., de Terlizzi, M., and Myrtle, T. F., "New Developments in Vibration Reduction with Actively Controlled Trailing Edge Flaps," *Mathematical and Computer Modelling*, Vol. 33, 2001, pp. 1055–1083. doi:10.1016/S0895-7177(00)00300-9

[20] Koratkar, N. A., and Chopra, I., "Wind Tunnel Testing of a Smart Rotor Model with Trailing Edge Flaps," *Journal of the American Helicopter Society*, Vol. 47, No. 4, Oct. 2002, pp. 263–272. doi:10.4050/JAHS.47.263

[21] Straub, F. K., Kennedy, D. K., Bomzalski, D. B., Hassan, A. A., Ngo, H., Anand, V. R., and Birchette, T. S., "Smart Material Actuated Rotor Technology—SMART," *Journal of Intelligent Material Systems and Structures*, Vol. 15, No. 4, April 2004, pp. 249–260. doi:10.1177/1045389X04042795

[22] Patt, D., Liu, L., and Friedmann, P. P., "Simultaneous Vibration and Noise Reduction in Rotorcraft Using Aeroelastic Simulation," *Journal of the American Helicopter Society*, Vol. 51, No. 2, April 2006, pp. 127–140. doi:10.4050/JAHS.51.127

[23] Dieterich, O., Enenkl, B., and Roth, D., "Trailing Edge Flaps for Active Rotor Control Aeroelastic Characteristics of the ADASYS Rotor System," *Proceedings of the 62nd American Helicopter Society Annual Forum*, AHS International, Alexandria, VA, May 2006, pp. 1–22.

[24] Saberi, H., Khoshlahjeh, M., Ormiston, R. A., and Rutkowski, M. J., "Overview of RCAS and Application to Advanced Rotorcraft Problems," *Proceedings of the American Helicopter Society 4th Decennial Specialist's Conference on Aeromechanics*, AHS International, Alexandria, VA, Jan. 2004, pp. 1–41.

[25] Johnson, W., "Rotorcraft Dynamics Models for a Comprehensive Analysis," *Proceedings of the 54th Annual Forum of the American Helicopter Society*, AHS International, Alexandria, VA, May 1998, pp. 1–21.

[26] Bir, G., Chopra, I., and Nguyen, K., "Development of UMARC (University of Maryland Advanced Rotor Code)," *American Helicopter Society 46th Annual Forum Proceedings*, AHS International, Alexandria, VA, May 1990, pp. 55–78.

[27] Rogers, K. L., "Airplane Math Modeling Methods for Actively Control Design," AGARD CP-228, Rhode-Saint-Genèse, Belgium, Aug. 1977.

[28] Edwards, J. H., "Application of Laplace Transform Methods to Airfoil Motion and Stability Calculations," 20th AIAA Structures, Structural Dynamics and Materials Conf., St. Louis, MO, AIAA Paper 1979-772, April 1979.

[29] Karpel, M., "Design for Active and Passive Flutter Suppression and Gust Alleviation," NASA CR 3492, Nov. 1981.

[30] Vepa, R., "Finite State Modeling of Aeroelastic Systems," NASA CR 2779, 1977.

[31] Myrtle, T. F., and Friedmann, P. P., "Application of a New Compressible Time Domain Aerodynamic Model to Vibration Reduction in Helicopters Using an Actively Controlled Flap," *Journal of the American Helicopter Society*, Vol. 46, No. 1, Jan. 2001, pp. 32–43. doi:10.4050/JAHS.46.32

[32] Glaz, B., Friedmann, P. P., Liu, L., Kumar, D., and Cesnik, C. E. S., "The AVINOR Aeroelastic Simulation Code and Its Application to Reduced Vibration Composite Rotor Blade Design," 50th AIAA/ASME/ASCE/AHS/ACS Structures, Structural Dynamics and Materials Conf., Palm Springs, CA, AIAA Paper 2009-2601, May 2009.

[33] Liu, L., Friedmann, P. P., Kim, I., and Bernstein, D. S., "Rotor Performance Enhancement and Vibration Reduction in Presence of Dynamic Stall Using Actively Controlled Flaps," *Journal of the American Helicopter Society*, Vol. 53, No. 4, Oct. 2008, pp. 338–350. doi:10.4050/JAHS.53.338

[34] Peroomian, O., Chakravarthy, S., Palaniswamy, S., and Goldberg, U., "Convergence Acceleration for Unified-Grid Formulation Using Preconditioned Implicit Relaxation," AIAA Paper 98-0116, Jan. 1998.

[35] Peroomian, O., Chakravarthy, S., and Goldberg, U., "A 'Grid-Transparent' Methodology for CFD," AIAA Paper 97-0724, Reno, NV, Jan. 1997.

[36] Chakravarthy, S. R., and Osher, S., "New Class of High Accuracy TVD Schemes for Hyperbolic Conservation Laws," 23rd AIAA Aerospace Sciences Meeting and Exhibit, Reno, NV, AIAA Paper 85-0363, Jan. 1985.

[37] Menter, F. R., "Two-Equation Eddy-Viscosity Turbulence Models for Engineering Applications," *AIAA Journal*, Vol. 32, No. 8, Aug. 1994, pp. 1598–1605. doi:10.2514/3.12149

[38] Thiel, M. R., Lesieutre, G. A., Maughmer, M. D., and Koopmann, G. H., "Actuation of an Active Gurney Flap for Rotorcraft Applications," 47th AIAA/ASME/ASCHE/AHS/ASC Structures, Structural Dynamics & Materials Conf., Newport, RI, AIAA Paper 2006-2181, May 2006.

[39] Liu, L., Friedmann, P. P., and Padthe, A. K., "An Approximate Unsteady Aerodynamic Model for Flapped Airfoils Including Improved Drag Predictions," *Proceedings of the 34th European Rotorcraft Forum*, Royal Aeronautical Society, London, Sept. 2008.

[40] Li, Y., Wang, J., and Zhang, P., "Influences of Mounting Angles and Locations on the Effects of Gurney Flaps," *Journal of Aircraft*, Vol. 40, No. 3, May–June 2003, pp. 494–498. doi:10.2514/2.3144

[41] Abbott, I. H., and Doenhoff, A. E. V., *Theory of Wing Sections*, Dover, New York, 1959.

[42] de Terlizzi, M., and Friedmann, P. P., "Active Control of BVI Induced Vibrations Using a Refined Aerodynamic Model and Experimental Correlation," *American Helicopter Society 55th Annual Forum Proceedings*, AHS International, Alexandria, VA, May 1999, pp. 599–615.

[43] Liu, L., Friedmann, P. P., and Padthe, A. K., "Comparison of Approximate Time Domain Aerodynamics for Flapped Airfoils with CFD Based Results with Applications," *Proceedings of the AHS Specialists' Conference on Aeromechanics*, AHS International, Alexandria, VA, Jan. 2008, pp. 1–17.

[44] Rodden, W. P., and Albano, E., "A Doublet-Lattice Method for Calculating Lift Distributions on Oscillating Surfaces in Subsonic Flows," *AIAA Journal*, Vol. 7, No. 2, Feb. 1969, pp. 279–285. doi:10.2514/3.5086

[45] Bisplinghoff, R. L., Ashley, H., and Halfman, R., *Aeroelasticity*, Addison-Wesley, Reading, MA, 1955, Chap. 6, pp. 317–325.

[46] Allwine, D. A., Strahler, J. A., Lawrence, D. A., Jenkins, J. E., and Myatt, J. H., "Nonlinear Modeling of Unsteady Aerodynamics at High Angle of Attack," *AIAA Atmospheric Flight Mechanics Conference and Exhibit*, Providence, RI, Aug. 2004, 1–18.

[47] Lee, D., Leishman, J. G., and Baeder, J. D., "A Nonlinear Indicial Method for the Calculation of Unsteady Airloads," *Proceedings of the 59th American Helicopter Society Annual Forum*, AHS International, Alexandria, VA, May 2003, 1–28.

[48] Jeffrey, D., Zhang, X., and Hurst, D. W., "Aerodynamics of Gurney Flaps on a Single-Element High-Lift Wing," *Journal of Aircraft*, Vol. 37, No. 2, 2000, pp. 295–301. doi:10.2514/2.2593

[49] Millott, T. A., and Friedmann, P. P., "Vibration Reduction in Helicopter Rotors Using an Actively Controlled Partial Span Trailing Edge Flap Located on the Blade," NASA CR 4611, June 1994.

[50] Patt, D., Liu, L., and Friedmann, P. P., "Active Flaps for Noise Reduction: A Computational Study," *American Helicopter Society 61st Annual Forum Proceedings*, AHS International, Alexandria, VA, June 2005, pp. 1–21.

[51] Patt, D., Liu, L., Chandrasekar, J., Bernstein, D. S., and Friedmann, P. P., "Higher-Harmonic-Control Algorithm for Helicopter Vibration Reduction Revisited," *Journal of Guidance, Control, and Dynamics*, Vol. 28, No. 5, Sept.–Oct. 2005, pp. 918–930. doi:10.2514/1.9345

B. Balachandran
Deputy Editor